# FABRICATION AND CHARACTERIZATION OF InGaN BASED SOLAR CELL: FROM MATERIAL TO DEVICE

# **AHMAD SAUFFI BIN YUSOF**

UNIVERSITI SAINS MALAYSIA

# FABRICATION AND CHARACTERIZATION OF InGaN BASED SOLAR CELL: FROM MATERIAL TO DEVICE

by

# **AHMAD SAUFFI BIN YUSOF**

Thesis submitted in fulfilment of the requirements for the degree of Doctor of Philosophy

January 2024

#### ACKNOWLEDGEMENT

The journey to completing this thesis as a student under the co-tutelle (dual-PhD) program between Universiti Sains Malaysia (USM), Malaysia and Université de Lorraine (UL), France, has been wonderful and adventurous. I want to express my gratitude to the individuals and institutions supporting me. Their guidance and inspiration have been invaluable. First and foremost, I extend my most profound appreciation to my thesis advisors, Prof. Dr. Zainuriah HASSAN from USM and Prof. Dr. Sidi HAMADY from UL. Your combined expertise, wisdom, and dedication to my academic journey have been instrumental in shaping this research. Your guidance and mentorship have been a constant source of inspiration, and I am truly grateful for your unwavering support. I also want to acknowledge the contributions of my co-thesis advisor, Assoc. Prof. Dr. Sha Shiong NG for his insightful feedback and constructive criticism, which significantly improved the quality of this work. I would also like to extend my gratitude to the esteemed examination committee members for their expertise and valuable insights during the evaluation of this thesis. I am profoundly thankful to Anas AHMAD and the entire team at INOR, USM, and Queny KIEFFER, along with the whole team at LMOPS, UL, for fostering an environment that nurtures intellectual curiosity and providing the essential resources and infrastructure for this adventurous quest. I also wish to acknowledge the French Embassy in Malaysia, UL, and USM for their financial support. I want to acknowledge my family for their unwavering support, love, and encouragement. Your belief in me has been my driving force, and I am deeply thankful for everything you have done for me. Thank you also for being there during the ups and downs of this journey. Lastly, I dedicate this thesis to my mother, whose memory has been a constant source of inspiration and motivation.

#### TABLE OF CONTENTS

ACK	NOWLE	DGEMENT	ii
TAB	LE OF CO	ONTENTS	iii
LIST	OF TAB	LES	vii
LIST	OF FIGU	URES	viii
LIST	OF SYM	BOLS	xiv
LIST	OF ABB	REVIATIONS	xvi
LIST	OF APP	ENDICES	xviii
ABS	TRAK		xix
ABS	TRACT		xxi
СНА	PTER 1	CONTEXT AND OBJECTIVES	1
1.1	Problem	statement of InGaN-based solar cell	1
1.2	Research	n objectives	6
1.3	Research	n originality	7
1.4	Research	n scope	8
1.5	Thesis o	utline	9
_	APTER 2 ERATURI	InGaN FOR OPTOELECTRONICS AND PHOTOE REVIEW	
2.1	InGaN n	naterial systems for solar cells applications	11
	2.1.1	Crystal structure	12
	2.1.2	Physical properties	19
	2.1.3	Limitations and challenges	22
		2.1.3(a) Growth process	22
		2.1.3(b) Substrate	31
	2.1.4	Defect mechanisms	34
		2.1.4(a) Point defect	35

		2.1.4(b) Linear defect	38
		2.1.4(c) Planar defect	41
2.2	Metal-se	emiconductor junction	43
	2.2.1	Schottky junction	44
	2.2.2	Current transport mechanism	47
	2.2.3	Development of InGaN-based Schottky devices	50
2.3	State-of	-the-art InGaN-based solar cells	54
	2.3.1	InGaN-based thick solar cells	58
	2.3.2	InGaN-based MQWs solar cells	61
	2.3.3	InGaN-based Schottky solar cells	64
_	PTER 3 LEMENT	InGaN GROWTH AND CHARACTERIZATI ED EXPERIMENTAL PROCEDURES	
3.1	MOCVI	D technique	68
	3.1.1	Basic principle and reactor design of TNSC SR-4000 MOCVD system	69
	3.1.2	MOCVD growth mechanics	72
	3.1.3	MOCVD growth process	80
3.2	Fabricat	ion techniques	81
	3.2.1	Sample preparation	81
	3.2.2	Deposition process	83
	3.2.3	Post-annealing treatment	84
3.3	Characte	erization techniques	85
	3.3.1	High-Resolution X-ray Diffraction (HR-XRD)	85
	3.3.2	Field Emission Scanning Electron Microscopy (FE-SEM)	88
	3.3.3	Atomic Force Microscopy (AFM)	91
	3.3.4	Ultraviolet visible near-infrared (UV-Vis-NIR) spectro- photometry	93
	3.3.5	Photoluminescence (PL)	96

	3.3.6	Photocurrent spectroscopy	98
	3.3.7	Electrical characterization	99
	PTER 4 SE InGaN	GROWTH AND EXPERIMENTAL STUDY OF S N MATERIAL	
4.1	Introduc	ction	102
4.2	InGaN r	material study	104
	4.2.1	Experimental details	104
	4.2.2	Structural analysis	106
	4.2.3	Morphology analysis	111
	4.2.4	Optical analysis	117
	4.2.5	Electrical analysis	120
		4.2.5(a) Characterization procedure	121
		4.2.5(b) Two-layer model	124
		4.2.5(c) Application to InGaN/GaN heterostructure	128
4.3	InGaN growth for device fabrication		
	4.3.1	Experimental details	133
	4.3.2	Material characterization	135
4.4	Summar	ry	141
_	PTER 5	FABRICATION AND STUDY OF InGaN-BASED SCH	
5.1	Introduc	ction	144
5.2	Experim	nental details	145
5.3	I-V-T m	neasurement	147
	5.3.1	I-V-T characteristic curve	147
	5.3.2	Schottky diode characteristic parameters	150
	5.3.3	Analysis of inhomogeneous barrier height	153
	5.3.4	Modified Richardson plot	157
5.4	Photocu	Photocurrent measurement	

5.5	Summary	<i>I</i>	165
СНАР	TER 6	CONCLUSION AND FUTURE RECOMMENDATIONS	167
6.1	Conclusion	on	167
6.2	Recomm	endations for future research	170
	6.2.1	Material development	170
	6.2.2	Device fabrication	171
REFE	RENCES		173
APPE	NDICES		

#### LIST OF TABLES

	Page
Table 2.1	III-nitride lattice parameter
Table 2.2	Physical properties related to the binary of III-nitride21
Table 2.3	Crystal defects classifications
Table 2.4	Reports on the development In <sub>x</sub> Ga <sub>1-x</sub> N-based Schottky devices52
Table 2.5	Work function and electron negativity of some common metals53
Table 2.6	Reports on In <sub>x</sub> Ga <sub>1-x</sub> N-based solar cell performance55
Table 4.1	MOCVD growth parameters of the $In_xGa_{1-x}N/GaN$ heterostructure
Table 4.2	The thickness and electrical properties of the ud-GaN structure 133
Table 4.3	MOCVD growth parameters of the $In_xGa_{1-x}N/GaN$ heterostructure
Table 4.4	The obtained indium composition of the In <sub>x</sub> Ga <sub>1-x</sub> N epilayer
	through XRD, transmittance and PL measurements142
Table 5.1	Calculated value of $\bar{\phi}_{B_0}$ and $\sigma_s$ obtained from the $\phi_{ap}$ plot as a
	function of $q/2k_BT$
Table 5.2	Calculated value of $\rho_3$ and $\rho_2$ obtained from the $n^{-1}-1$ plot as a
	function of $q/2k_BT$
Table 5.3	Calculated value of $\bar{\phi}_{B_Q}$ and $A^*$ obtained from the modified
	Richardson plot as a function of $q/k_BT$ 160
Table 5.4	The obtained indium composition of the In <sub>x</sub> Ga <sub>1-x</sub> N epilayer
	through XRD, transmittance and photocurrent measurement166

#### LIST OF FIGURES

	Page
Figure 2.1	Crystal structure of GaN polytypes with its different stacking sequence: (a) wurtzite ( <i>P</i> 63 <i>mc</i> space group with <i>C</i> 6 <i>v</i> 4 symmetry) and (b) zinc-blende ( <i>F</i> 43 <i>m</i> space group with <i>Td</i> 2 symmetry)13
Figure 2.2	Crystal structure of InGaN polarity: (a) III-polar and (b) N-polar16
Figure 2.3	AM0 solar spectrum as a function of spectral wavelength and its correlation with InGaN bandgap (from 0.7 eV (1770 nm) to 3.4 eV (360 nm)), showing that this ternary is almost perfectly matched with the solar spectrum simply by manipulating indium composition
Figure 2.4	(a) Calculated valence and conduction band curve of InN based on theoretical k.p model and (b) experimental and absorption edge of InN following the experimental and theoretical value according to parabolic and non-parabolic conduction band
Figure 2.5	The E <sub>FS</sub> position in relation to conduction band maxima and valence band minima of GaN, InN, GaAs and Ga <sub>0.5</sub> In <sub>0.5</sub> P20
Figure 2.6	Phase diagram proposed by Stringfellow considering fully relaxed InGaN structure; dotted line represent spinodal line, while solid line represent binodal line
Figure 2.7	The spinodal decomposition region of InGaN as a function of its strain from fully relaxed to fully strained with respect GaN template
Figure 2.8	Equilibrium vapor pressure of N <sub>2</sub> over AlN, GaN and InN27
Figure 2.9	Conversion efficiency of $NH_3$ in a quartz reactor (with and without stainless steel enclosure) at 1 atm for different temperature range 28
Figure 2.10	Growth transition between low and high V/III ratio in relation to NH <sub>3</sub> flow

Figure 2.11	Surface and cross-section image of the indium droplets formation	
	on the surface of In <sub>0.29</sub> Ga <sub>0.71</sub> N structure	.30
Figure 2.12	Summary of process-induced related defects	.30
Figure 2.13	Ball-stick model of GaN structure	.32
Figure 2.14	Compressive (a) and tensile (b) strained layers (red atoms) on a substrate (green atoms)	
Figure 2.15	Schematic diagram of surface charges, direction of electric field and polarization field for spontaneous and piezoelectric polarization in III-nitrides for Ga- and N-face orientations	.34
Figure 2.16	Formation path of nitrogen passivation mechanism	.38
Figure 2.17	(a) Burgers vector direction as a function of dislocation type and (b) schematic representation of dislocations component within the crystal lattice	.40
Figure 2.18	(a) Schematic representation of surface pit formation induced by screw type dislocation component theoretically predicted by Frank model and (b) experimental observation of the pit formation on the GaN surface through SEM measurement	.40
Figure 2.19	The basal stacking faults model with its respective stacking sequences, where <i>R</i> is the stacking fault displacement vector	.42
Figure 2.20	Energy band diagram of metal and n-type semiconductor in isolation and in contact with each other (at thermal equilibrium)	
Figure 2.21	Energy band diagram of Schottky junction under (a) forward bias and (b) reverse bias. (c) Typical I-V characteristics of Schottky junction under forward and reverse bias	.47
Figure 2.22	Schematics representation of carrier transport mechanism of Schottky junction at different doping level	.48
Figure 2.23	Schematic representation of (a) transverse and (b) co-planar structure	.50
Figure 2.24	Bandgap energy and work function of In <sub>x</sub> Ga <sub>1-x</sub> N as a function of indium composition	

Figure 2.25	The state-of-art InGaN-based solar cell the structure with a thick
	InGaN active layer; (a) p-n homojunction, (b) p-i-n homojunction
	and (c) p-i-n heterojunction59
Figure 2.26	The InGaN-based solar cell the structure with a MQWs InGaN
	active layer62
Figure 2.27	The schematic representation of InGaN-based Schottky solar cells
	65
Figure 3.1	Simplified schematic layout of TNSC SR-4000 MOCVD system70
Figure 3.2	Summary of GaN growth route through the gas-phase reaction
	(direct pyrolysis and adduct) between TMGa and NH <sub>3</sub> 73
Figure 3.3	(a) Ball-stick model of TEGa structure and (b) TEGa structure and
	the energetic reaction during first $\beta$ -hydride elimination process76
Figure 3.4	Simplified GaN growth mechanism using MOCVD technique77
Figure 3.5	Schematic of the three different temperature regimes for the
	MOCVD growth process
Figure 3.6	Samples cleaning procedure prior metallization process
Figure 3.7	Summary of the fabrication process.
Figure 3.8	(a) Visualization of the Braggs diffraction in periodic crystal
	structure and (b) scan geometry in HR-XRD, where S is the
	scattering vector and Q is surface normal87
Figure 3.9	(a) Electron-induce emission signal and (b) characteristic of X-ray
	emission90
Figure 3.10	(a) Schematic illustration of typical AFM configuration and (b)
	force regimes governing the AFM measurement based on Lennard-
	Jones potential
Figure 3.11	Schematic illustration of simplified spectrophotometer system
	with dual beam configuration94
Figure 3.12	Radiative and nonradiative transition mechanism97
Figure 3.13	Schematic illustration of the MPC system99

Figure 4.1	Schematic representations of the grown In <sub>x</sub> Ga <sub>1-x</sub> N/GaN
	heterostructure
Figure 4.2	Temperature profile of the $In_xGa_{1-x}N/GaN$ heterostructure growth
	process using MOCVD technique. THC and LTBL denote thermal
	hydrogen cleaning and low temperature buffer layer, respectively .105
Figure 4.3	XRD diffractograms of the grown $In_xGa_{1-x}N/GaN$ heterostructure
	as a function of In <sub>x</sub> Ga <sub>1-x</sub> N growth temperature107
Figure 4.4	Summary of peaks properties and extracted value of lattice
	parameters and indium composition
Figure 4.5	RSM image of In <sub>x</sub> Ga <sub>1-x</sub> N/GaN heterostructure as a function of
	$In_xGa_{1-x}N$ growth temperature scanned at $(10\overline{1}5)$ reflection111
Figure 4.6	FE-SEM image of the grown In <sub>x</sub> Ga <sub>1-x</sub> N/GaN heterostructure as a
	function of $In_xGa_{1-x}N$ growth temperature: (a) ud-GaN, (b) 860 °C,
	(c) 840 °C, and (d) 820 °C112
Figure 4.7	FE-SEM cross-section image of the grown In <sub>x</sub> Ga <sub>1-x</sub> N/GaN
	heterostructure as a function of $In_xGa_{1-x}N$ growth temperature: (a)
	ud-GaN, (b) 860 °C, (c) 840 °C, and (d) 820 °C115
Figure 4.8	AFM images of In <sub>x</sub> Ga <sub>1-x</sub> N/GaN heterostructure as a function of
	$In_xGa_{1-x}N$ growth temperature: (a) ud-GaN, (b) 860 °C, (c) 840 °C,
	and (d) 820 °C
Figure 4.9	Summary of (a) surface roughness and (b) height profile of $In_xGa_1$ -
	xN/GaN heterostructure (scanned along red arrow direction in
	Figure 4.8) as a function of In <sub>x</sub> Ga <sub>1-x</sub> N growth temperature117
Figure 4.10	(a) Transmittance spectra and (b) calculated Tauc plot of the
	$In_xGa_{1-x}N/GaN$ heterostructure as a function of $In_xGa_{1-x}N$ growth
	temperature
Figure 4.11	Room temperature normalized PL spectra of $In_xGa_{1-x}N/GaN$
	heterostructure as a function of In <sub>x</sub> Ga <sub>1-x</sub> N growth temperature120

Figure 4.12	Configuration of (a) van der Pauw and (b) Hall effect measurement
	for determining the resistivity and carrier concentration of the
	grown In <sub>x</sub> Ga <sub>1-x</sub> N/GaN heterostructure
Figure 4.13	(a) Van der Pauw voltage, (b) Hall voltage with respect to the applied magnetic field orientation, (c) resistivity, (d) carrier concentration and mobility of the grown In <sub>0.04</sub> Ga <sub>0.96</sub> N/GaN heterostructure and the In <sub>0.04</sub> Ga <sub>0.96</sub> N epilayer extracted through experimental measurement and two-layer model, respectively, as a function of injected current
Figure 4.14	The resistivity, carrier concentration and mobility value of the grown $In_xGa_{1-x}N/GaN$ heterostructure and the $In_xGa_{1-x}N$ epilayer extracted through experimental measurement and two-layer model, respectively
Figure 4.15	Schematic representations of the grown In <sub>x</sub> Ga <sub>1-x</sub> N/GaN heterostructure
Figure 4.16	Temperature profile of the $In_xGa_{1-x}N/GaN$ heterostructure growth process using MOCVD technique. THC and LTBL denote thermal hydrogen cleaning and low temperature buffer layer, respectively .135
Figure 4.17	XRD diffractograms of the grown $In_xGa_{1-x}N/GaN$ heterostructure with the $In_xGa_{1-x}N$ epilayer grown at 860 °C and 840 °C. The diffractograms also show GaN-TEG epilayer grown at 860 °C136
Figure 4.18	RSM image of $In_xGa_{1-x}N/GaN$ heterostructure with the $In_xGa_{1-x}N$ epilayer grown at (a) 860 °C and (b) 840 °C
Figure 4.19	FE-SEM image of the (a) GaN-TEG and $In_xGa_{1-x}N$ epilayer grown at (b) 860 °C and (c) 840 °C139
Figure 4.20	FE-SEM cross-section image of the (a) GaN-TEG/GaN with the GaN-TEG epilayer grown at 860 °C and $In_xGa_{1-x}N/GaN$ heterostructure with the $In_xGa_{1-x}N$ epilayer grown at (b) 860 °C and (c) 840 °C
Figure 4.21	(a) Transmittance spectra and (b) calculated Tauc plot of the GaN-TEG/GaN with the GaN-TEG epilayer grown at 860 °C and

	at 860 °C and 840 °C	141
Figure 5.1	FE-SEM cross-section image of Ti/Al contact deposited on glass substrate	146
Figure 5.2	Surface and 3D optical profilometer image of Pt contact deposited on $In_xGa_{1-x}N/GaN$ heterostructure	147
Figure 5.3	Semilog forward and reverse bias I-V characteristics of Pt/GaN and Pt/In $_x$ Ga $_{1-x}$ N Schottky barrier diode in the temperate range of 90-300 K	148
Figure 5.4	The extracted value of ideality factor and barrier height of Pt/GaN and $Pt/In_xGa_{1-x}N$ Schottky barrier diode as a function of measurement temperature	152
Figure 5.5	Schematic representation of $Pt/In_xGa_{1-x}N$ interface with Schottky barrier inhomogeneity	154
Figure 5.6	Zero bias apparent barrier height and ideality factor function $(n^{-1}-1)$ plot as a function of $q/2k_BT$ with the linear fit according to Gaussian distribution of barrier height	156
Figure 5.7	The modified Richardson plot as a function of $q/k_BT$ of the fabricated Pt/GaN and Pt/In <sub>x</sub> Ga <sub>1-x</sub> N Schottky barrier diode following the Gaussian distribution of barrier height	160
Figure 5.8	Photocurrent spectra of the fabricated $In_xGa_{1-x}N/GaN$ heterostructure in co-planar configurations; the incident excitation is incident from the $In_xGa_{1-x}N$ (front) side	163
Figure 5.9	Photocurrent spectra of the fabricated In <sub>x</sub> Ga <sub>1-x</sub> N/GaN heterostructure in co-planar configurations; the incident excitation is incident from the GaN (back) side	164

#### LIST OF SYMBOLS

Α Diode area  $A^*$ Richardson constant In-pane lattice constant а В Magnetic flux Burger's vector b Out-of-plane lattice constant С d Thickness Reciprocal lattice spacing for the (hkl) plane  $d_{hkl}$  $E_F$ Fermi energy  $E_{a}$ Energy bandgap  $E_{\infty}$ Tunneling parameter h. Planck's constant  $I_{s}$ Reverse saturation current  $I_{sc}$ Short-circuit current Short-circuit current density  $J_{sc}$  $k_B$ Boltzmann constant  $m_0$ Free electron mass n Carrier concentration Oxygen substitutional  $O_N$ Q Flow rate Electron charge q R Resistance Series resistance  $R_s$ Т Temperature t Thickness  $V_{bi}$ Build-in potential  $V_H$ Hall voltage  $V_N$ Nitrogen vacancy  $V_{oc}$ Open circuit voltage Absorption coefficient α

Bowing parameter

b

$\phi$	Barrier height
σ	Conductivity
μ	Mobility
η	Correction factor
n	Ideality factor
ρ	Resistivity
λ	Wavelength
$\theta$	X-ray angle

#### LIST OF ABBREVIATIONS

AFM Atomic force microscope

AlN Aluminum nitride

a.u. Arbitrary unit

BSF Basal plane stacking fault CBM Conduction band minima

DLTS Deep-level transient spectroscopy

E-beam Electron beam

ESB Ehrlich-Schwoebel barrier

EQE External quantum efficiency

FE Field emission

FE-SEM Field emission scanning electron microscope

FWHM Full width at half maximum

GaN Gallium nitride

HCP Hexagonal close-packed

HEMT High electron mobility transistor

InGaN Indium gallium nitride

LD Laser diode

LTBL Low temperature buffer layer

MBE Molecular-beam epitaxy

MFC Mass flow controller

MO Metal organic

MOCVD Metal organic chemical vapor deposition

MQW Multiple quantum well

NIR Near-infrared

PC Pressure controller

PCE Power conversion efficiency

PL Photoluminescence

QB Quantum barrier

QCSE Quantum-confined stark effect

RLP Reciprocal lattice point

RMS Root-mean-square

RSM Reciprocal space map

RT Room temperature

SBH Schottky barrier height

SCCM Standard cubic centimeters per minute

Si Silicon

SiC Silicon carbide

SLs Superlattice structure

SLM Standard liter per minute

TE Thermionic emission

TEGa Triethylgallium

TFE Thermionic field emission

THC Thermal hydrogen cleaning

TMGa Trimethylgallium
TMIn Trimethylindium

Ud-GaN Unintentionally doped gallium nitride

UV Ultra-violet

VBM Valence band maxima

Vis Visible

XRD X-ray diffraction

ZnO Zinc oxide

#### LIST OF APPENDICES

APPENDIX A PHOTOCURRENT AND SPECTRAL RESPONSE OF SILICON PHOTODIODE (MODEL: NEWPORT 818-UV-L)

# FABRIKASI DAN PENCIRIAN SEL SOLAR BERASASKAN InGaN: DARI BAHAN KE PERANTI

#### **ABSTRAK**

Sistem bahan indium galium nitrida (InGaN) telah muncul sebagai calon yang berpotensi untuk sel solar berkecekapan tinggi kerana sifat intrinsiknya. Bagaimanapun, pembangunan sel solar berasaskan InGaN menghadapi beberapa cabaran, termasuk keperluan lapisan dopan-p dan penghasilan aloi InGaN yang berkualiti tinggi dengan kandungan indium yang tinggi. Kajian ini meneroka strategi inovatif untuk mengatasi cabaran tersebut, dengan fokus kepada pembangunan praktikal sel solar Schottky berasaskan lapisan In<sub>x</sub>Ga<sub>1-x</sub>N yang tebal, dari pertumbuhan hingga pencirian peranti. Untuk pembangunan bahan, siri pertumbuhan In<sub>x</sub>Ga<sub>1-x</sub>N/ GaN telah dijalankan pada substrat c-satah nilam menggunakan pemendapan wap kimia logam-organik (MOCVD) pada pelbagai suhu pertumbuhan. Pelbagai teknik pencirian digunakan, termasuk belauan sinar-X (XRD), mikroskopi imbasan elektron pancaran medan (FE-SEM), mikroskopi daya atomik (AFM), fotopendarcahayaan (PL), and pengukuran kesan Hall untuk menilai sifat struktur, morfologi, optik, dan elektrik untuk struktur In<sub>x</sub>Ga<sub>1-x</sub>N. Analisis XRD menunjukkan puncak In<sub>x</sub>Ga<sub>1-x</sub>N dan GaN yang dikesan dengan baik tanpa bukti pemisahan fasa atau ketidakseragaman komposisi. Anggaran komposisi indium dari analisis XRD berjulat dari 4.02% hingga 10.86% untuk pelbagai suhu pertumbuhan, yang disahkan oleh analisis transmisi dan PL. Analisis permukaan menunjukkan pembentukan liang-V dengan peningkatan komposisi indium akibat pergerakan adatom yang berkurang pada suhu pertumbuhan yang lebih rendah. Pencirian elektrik memperkenalkan model dua lapisan baru untuk mengekstrak sifat lapisan In<sub>x</sub>Ga<sub>1-x</sub>N, yang mendedahkan kepekatan pembawa yang tinggi disebabkan oleh kekosongan nitrogen dan penurunan mobiliti bagi komposisi indium yang lebih tinggi disebabkan oleh penurunan struktur kualiti, selaras dengan analisis XRD dan AFM/FE-SEM. Dalam kajian peranti, diod Schottky berasaskan In<sub>x</sub>Ga<sub>1-x</sub>N dengan sentuhan platinum telah difabrikasi untuk aplikasi sel solar. Pengukuran arus-voltan-suhu (I-V-T) dan fotoarus telah dijalankan. Ketinggian halangan Schottky menunjukkan dua taburan Gaussian dalam rejim suhu tertentu, menunjukkan kehadiran ketidakseragaman ketinggian halangan antara muka diod. Pada kawasan suhu yang lebih tinggi (>150 K), nilai purata ketinggian halangan berjulat dari 1.29 eV hingga 0.90 eV, berkurangan dengan komposisi indium, selaras dengan model Mott-Schottky kerana In<sub>x</sub>Ga<sub>1-x</sub>N dengan komposisi indium yang lebih tinggi akan memiliki fungsi kerja yang lebih tinggi. Pencirian fotoarus menunjukkan puncak kecekapan kuantum luaran (EQE) sebanyak 55.03% pada 373 nm untuk peranti Pt/In<sub>0.05</sub>Ga<sub>0.95</sub>N Schottky. Bagaimanapun, peningkatan komposisi indium menyebabkan nilai EQE yang lebih rendah, selaras dengan penurunan kualiti bahan yang diperhatikan dalam pelbagai analisis. Walaupun nilai EQE yang lebih rendah, peranti menunjukkan spektrum penyerapan sel solar yang lebih luas, dari 360 nm ke panjang gelombang melebihi 400 nm, menunjukkan potensi bahan In<sub>x</sub>Ga<sub>1-x</sub>N untuk aplikasi fotovoltan. Kajian ini menekankan kebolehan menggunakan diod Schottky berdasarkan InGaN untuk aplikasi sel solar dan memberikan pandangan untuk meningkatkan kecekapannya.

# FABRICATION AND CHARACTERIZATION OF InGaN BASED SOLAR CELL: FROM MATERIAL TO DEVICE

#### **ABSTRACT**

Indium gallium nitride (InGaN) material system has emerged as a promising candidate for high-efficiency solar cells due to its exceptional intrinsic properties. However, developing InGaN-based solar cells faces several challenges, including needing a p-doped layer and producing high-quality indium-rich InGaN alloy. This study explores innovative strategies to overcome these challenges, focusing on the practical development of thick In<sub>x</sub>Ga<sub>1-x</sub>N-based Schottky solar cells, from material growth to device characterization. For material development, an In<sub>x</sub>Ga<sub>1-x</sub>N/GaN epitaxial growth was conducted on a c-plane sapphire substrate using metal-organic chemical vapor deposition (MOCVD) at various growth temperatures. Extensive characterization techniques, including X-ray diffraction (XRD), field-emission scanning electron microscopy (FE-SEM), atomic force microscopy (AFM), transmittance, photoluminescence (PL), and Hall Effect measurements, were employed to assess structural, morphological, optical, and electrical properties of the In<sub>x</sub>Ga<sub>1-x</sub>N structure. XRD analysis revealed well-resolved In<sub>x</sub>Ga<sub>1-x</sub>N and GaN peaks without evidence of phase separation or composition inhomogeneity. Estimated indium compositions from XRD analysis ranged from 4.02% to 10.86% for different growth temperatures with transmittance, and PL measurements validated these findings. Surface analysis indicated V-pits formation with increased indium composition due to reduced adatom mobility at lower growth temperatures. Electrical characterization introduced a novel two-layer model to extract In<sub>x</sub>Ga<sub>1-x</sub>N epilayer properties, revealing high carrier concentrations attributed to nitrogen vacancies and

decreased mobility with higher indium composition due to decreased structural quality, consistent with XRD and AFM/FE-SEM analysis. In the device development study, In<sub>x</sub>Ga<sub>1-x</sub>N-based Schottky diodes with platinum metal contacts were fabricated for solar cell applications. Temperature-dependent current-voltage (I-V-T) and photocurrent measurements were conducted. The Schottky barrier height exhibited a dual Gaussian distribution in a specific temperature regime, suggesting the presence of spatial barrier inhomogeneity within the fabricated diode junction interface. At higher temperature region (> 150 K), the average barrier height value ranged from 1.29 eV to 0.90 eV decrease with indium composition, aligning with the Mott-Schottky model as In<sub>x</sub>Ga<sub>1-x</sub>N with higher indium composition will possess higher work function. Photocurrent measurements demonstrated a peak external quantum efficiency (EQE) of 55.03% at 373 nm for Pt/In<sub>0.05</sub>Ga<sub>0.95</sub>N Schottky device. However, increasing indium composition led to decreased EQE values, aligned with material quality degradation observed in various analyses. Despite lower EQE values, the devices displayed a broad solar cell absorption spectrum, from 360 nm to wavelengths beyond 400 nm, indicating the potential of In<sub>x</sub>Ga<sub>1-x</sub>N materials for photovoltaic applications. This study underscores the feasibility of utilizing InGaN-based Schottky diode for solar cell applications and offers insights into improving their performance.

# **CHAPTER 1**

# **Context and Objectives**

Extensive research efforts have been dedicated to group-III nitride semiconductors following awarding of the 2014 Nobel Prize in Physics to Isamu Akasaki, Hiroshi Amano, and Shuji Nakamura for their contributions to the development of GaN-based blue light-emitting diodes (LEDs). The study has yielded noteworthy advancements in the field of material technology, specifically in the exploration of novel growth techniques and epilayer structural engineering, which can be used to fine-tune the properties of group-III nitrides according to demanded applications. The desired outcome of these efforts is to enhance the performance and widen the functionality of fabricated devices, not only in LEDs applications but also in other domains, such as power devices and photovoltaic applications.

#### 1.1 Problem statement of InGaN-based solar cell

The evolution of semiconductor technology has been significantly propelled by III-nitride materials, notably the ternary alloy known as InGaN. Its pivotal role spans across modern electronic and photonic applications, primarily owing to its exceptional tunable wide direct bandgap properties [1]–[3]. InGaN stands out as a cornerstone in the advancement of high-efficiency LEDs and continuous laser diodes (LDs), courtesy of its unique ability to fine-tune the indium-to-gallium ratio, thereby adjusting its bandgap value. This dynamic feature enables InGaN to emit light across an extensive spectrum, encompassing wavelengths from ultraviolet (UV) through the visible range, including green wavelengths, and extending further into the red

spectrum [4], [5]. Such unparalleled adaptability in bandgap modulation positions InGaN as an exceptionally versatile material catering to various optoelectronic and power devices applications. Its versatile nature extends far beyond illuminating displays, sparking substantial interest in exploring alternative technological applications.

The utilization of a wide direct bandgap of group-III nitride semiconductors, especially its ternary alloy such as InGaN also, has been widely considered a viable alternative material for silicon (Si)-based photovoltaic devices, which is currently dominating the photovoltaic industry. Si has formed the backbone of the photovoltaic industry for decades due to its widespread availability and low environmental impact. The current highest reported laboratory efficiency of this first-generation photovoltaic cell (single junction monocrystalline and polycrystalline Si-based solar cells) is around ~26% [6]–[9], which is close to its theoretical limit at ~31% (Shockley-Queisser limit) [10]–[13]. However, one of the inherent limitations of crystalline Si stems from its intrinsic properties, specifically the indirect nature of its electronic bandgap.

This resulted in poor solar spectrum absorption, particularly in the long wavelength region. This constraint can be partially addressed by employing a relatively thick active layer, typically spanning from 100 to 500 µm [14]. Even though it can improve absorption, it can also lead to a rise in the amount of material and cost production, particularly in large-scale implementations. It can also cause the manufactured cells to be rigid and inflexible. The thick Si solar cells also face inevitable power conversion efficiency losses caused by non-radiative recombination of photoexcited charge carriers along their extended path towards the electrical contacts located at the edges of the cell. Furthermore, it is worth noting that single junction Si-based solar cells experience additional energy losses of nearly 50% when

subjected to the AM1.5 solar radiation spectra, notably due to the solar spectral mismatch (transmission of low energy photons and thermalization loss) [15].

Thus, the indirect electronic bandgap and limited coverage of the solar spectrum of Si have generated widespread attention to seek a new and diverse type of wide direct bandgap materials. One of the candidates is the group-III nitride semiconductors and their related alloys since they possess a wide direct bandgap. For instance, the bandgap of InGaN alloy can be engineered from 0.7 eV (InN) to 3.4 eV (GaN). This characteristic renders it as the only material among the III-V semiconductors, including III-nitride that exhibits a remarkable spectral matching with the solar spectrum. The absorption edge of InGaN can be fine-tuned to optimize the light absorption and the device efficiency simply by manipulating the indium composition.

Henceforth, this can open a possibility for InGaN to serve as a sole material system for the active layer in multi-junction photovoltaic technology that can absorb a broader range of the solar spectrum. InGaN also exhibits a notably higher absorption coefficient (10<sup>5</sup> cm<sup>-1</sup>) than other III-V materials [16], making it a promising candidate for developing thin film solar cells. Additionally, InGaN shows experimental carrier mobilities exceeding 300 cm<sup>2</sup>/Vs [17], exceptional resistance to extreme conditions with an operational temperature of up to 400 °C [18], [19], a remarkable tolerance to ionizing radiation with irradiation-induced degradation in photoluminescence intensity lower than 0.1 decade/10<sup>12</sup> MeV/g [20] with a predicted lifespan of over 30 years under solar storm proton irradiation [18] and demonstrates high chemical stability [21], enabling the operation of fabricated photovoltaic devices in hostile environments such as extraterrestrial applications.

Thus, the InGaN-based solar cells are anticipated to outperform their Si-based counterparts. However, the experimental energy conversion efficiency that has been reported thus far is still much below (< 0.9% for thick structure [22]) its theoretical value (> 20% [23], [24]). While InGaN has achieved outstanding breakthroughs for the past decades in the field of LED technology, the development of InGaN in photovoltaic applications is still lagging, primarily due to issues associated with its growth and fabrication process, especially In<sub>x</sub>Ga<sub>1-x</sub>N with high indium composition (x > 0.2). Typically, the development of InGaN-based devices is achieved through the epitaxial growth using metal-organic chemical vapor deposition (MOCVD) or molecular beam epitaxy (MBE) on sapphire (Al<sub>2</sub>O<sub>3</sub>), Si, or silicon carbide (SiC) substrate [25]–[28].

The utilisation of such foreign substrates presents a significant challenge owing to the considerable mismatch in lattice and thermal expansion coefficients between the substrate and the subsequently grown InGaN epilayer. The process of heteroepitaxial growth often results in the creation of a significant number of structural defects at the heterointerfaces, such as misfit, threading dislocation, and point defect. These defects tend to propagate vertically throughout the entire device structure and serve as a recombination centre for photoexcited electrons, subsequently decreasing the overall photovoltaic performance of the fabricated device. Besides, achieving a high-quality crystalline structure with an extensive indium content (x > 0.5) is crucial for the successful implementation of  $In_xGa_{1-x}N$  films in high-efficiency InGaN-based photovoltaic applications [29].

However, this goal poses significant challenges due to the tendency of epitaxially grown In-rich InGaN films to undergo phase separation and exhibit composition inhomogeneities. This phenomenon arises from the solid-phase

miscibility gap caused by the substantial mismatch between InN and GaN [30]. The miscibility gap occurs within a specific range of the alloy mixture, wherein the thermodynamically unstable InGaN alloy undergoes spontaneous spinodal decomposition into multiple thermodynamically stable phases. As a result, the In-rich phase is distributed non-homogeneously within the layer, hindering the indium incorporation process, and compromising the crystallinity quality of the grown InGaN epilayer.

Moreover, the current configuration of InGaN-based solar cells relies on a p-in architecture, in which an InGaN (bulk or MQWs) epilayer is interposed between an
n-GaN (Si-doped) layer and a p-GaN (Mg-doped) layer. However, this approach faces
a challenge in achieving high quality for both the InGaN and p-GaN layers. The quality
of the InGaN layer strongly depends on the growth temperature of the subsequent pGaN layer. The necessity of a high temperature growth operation (>1000 °C) for the
p-GaN layer is deemed challenging, as it can result in negative effects such as lattice
relaxation, indium desorption, and indium fluctuation within the InGaN layer.
Conversely, the quality of the p-GaN epilayer can deteriorate (increase in electrical
resistance and defects density) when grown at relatively low temperatures, limiting the
overall photovoltaic performance.

Despite notable progress in the epitaxial and fabrication process of III-nitride materials, no major controls have been established to date over the material parameters of grown GaN and its ternary alloy, InGaN. It is well known that in the III-nitride epitaxial process, there are significant variations or tolerance in the materials parameters from growth chamber to growth chamber or even in one growth chamber over a period of operation or during the subsequent fabrication process. This is due to the lack of a comprehensive understanding of the growth kinetics and fundamental

aspects of III-nitride materials. Some of the physical mechanisms related to the specific properties of III-nitride materials system are still unexplored, such as optical and electrical properties.

In order to achieve high-quality In-rich monocrystalline InGaN epilayers, it is essential to gain a thorough understanding of the factors that govern the fundamental properties of this material. This understanding will enable precise control and optimization in the growth and fabrication process. Therefore, extended research work needs to be done toward this direction in terms of design, fabrication, and optimization to provide a deep conceptual understanding of the material fabrication process and to facilitate the realization of InGaN-based solar cells.

### 1.2 Research objectives

The work presented in this thesis is dedicated to the practical development of novel InGaN Schottky structures for solar cell applications, spanning from the fundamental materials research to the final device implementation, which is accomplished through the following objectives:

- a) To investigate the effect of InGaN growth temperature on the indium incorporation process in growing InGaN/GaN heterostructure using the MOCVD technique.
- b) To study an in-depth electrical analysis of the epitaxially grown InGaN/GaN heterostructure and investigate its correlation with its structural, optical, and morphology properties as a function of indium composition.
- c) To investigate the diode properties and photovoltaic performance of the fabricated novel InGaN-based Schottky diode for solar cell application.

The first objective involves conducting InGaN/GaN epitaxial growth on a cplane sapphire substrate. The main parameter under investigation is the growth temperature of the InGaN epilayer, which is varied from 860 °C to 780 °C in step of 20 °C to manipulate the indium composition while keeping other growth parameters constant. The second objective involves the development of a novel two-layer model, facilitating the characterization of the electrical properties of the grown epilayer independently from the underlying conductive GaN layer. This analysis is correlated with various measurement techniques, including X-ray diffraction (XRD), transmittance, scanning electron microscopy (SEM), and photoluminescence (PL). The third objective involves developing a process to fabricate platinum (Pt)/InGaN Schottky barrier diodes using an electron beam (e-beam) technique. Main diode characteristics such as barrier height and ideality factor are systematically assessed through temperature-dependent current-voltage measurements. Additionally, the photovoltaic performance, particularly the external quantum efficiency (EQE) parameter of the fabricated device, is characterized using photocurrent measurements. Overall, this research spans from the growth of the InGaN epitaxial layers to the detailed analysis of their structural, morphology, optical and electrical properties, ultimately leading to the fabrication and evaluation of InGaN-based Schottky diodes for potential use in solar cell applications.

## 1.3 Research originality

Within the framework of this study, InGaN/GaN heterostructure with an indium composition of up to 10.86% has been successfully grown without any occurrence of phase separation or composition inhomogeneity. The grown structure also has been rigorously characterized to study its structural, morphology, optical and

electrical properties. For the electrical characterization, a novel two-layer model has been developed to effectively extract the electrical properties of the grown InGaN epilayer while eliminating any electrical contributions from the underlying GaN epilayer. Significantly, this model is not limited solely to InGaN/GaN structures but can be extended to other materials where an active layer is grown on a semiconducting substrate, including various III-nitride and III-V materials. Subsequently, using the optimized structure, the InGaN-based Schottky solar cell was successfully fabricated using Pt metal contact and thoroughly characterized to evaluate the device properties and photovoltaic performance. To date, only one publication has reported the practical realization of InGaN-based Schottky solar cells using Pt metal contact. Thus, this study signifies a significant contribution to fundamental material research and photovoltaic application, particularly in the context of InGaN-based Schottky structure.

### 1.4 Research scope

The study conducted within the scope of this thesis revolves around the practical development of InGaN-based Schottky structures for solar cell applications, encompassing fundamental materials research to the final device implementation. The material study phase involved the epitaxial growth processes of InGaN/GaN heterostructures using the MOCVD technique, primarily focusing on optimizing the InGaN growth temperature. Subsequently, the impact of the InGaN growth temperature on various aspects, including structural, surface morphology, optical, and electrical properties, was rigorously characterized.

Building upon the optimized structure, the fabrication of InGaN-based Schottky devices was carried out, involving the deposition of Pt metal contacts using the e-beam deposition technique. The optoelectronic properties of these fabricated

devices were extensively investigated to study their electrical transport characteristics and the photovoltaic properties, particularly the EQE parameters, through a comprehensive research approach involving temperature-dependent current-voltage and photocurrent measurements.

#### 1.5 Thesis outline

The content of this thesis is organized as follows, covering the practical development of novel InGaN Schottky structure in terms of growth, fabrication, and characterization:

Chapter 1 is the introductory chapter, which provides brief technical background information, a problem statement, and the objective of this thesis. Following the introduction, Chapter 2 comprehensively highlights the literature on the fundamental and theoretical properties of InGaN as a material system. The outline of the current development of InGaN in photovoltaic applications is also included in Chapter 2.

Chapter 3 provides an explanation of the developed procedure related to the development of InGaN in materials and devices, which includes sample preparation, MOCVD growth, metal contact deposition and post-deposition treatment. Chapter 3 also provides a brief description of the characterization methods and techniques that have been implemented in this thesis to study the properties of the grown and fabricated structure.

Research findings that have been obtained throughout this study using the experimental procedures developed during the thesis and detailed in Chapter 3 are displayed and discussed in **Chapter 4** and **Chapter 5**. Chapter 4 primarily focuses on material development and characterization, while Chapter 5 centres around the

material growth, fabrication, and characterization of the InGaN-based Schottky devices for solar cell applications. Finally, **Chapter 6** summarizes the work and avenues for future research and provides a brief conclusion to the thesis.

This thesis work was carried out as part of a scientific collaboration initiated in 2019 between LMOPS (Université de Lorraine and CentraleSupélec) and INOR (Universiti Sains Malaysia) with a PHC ("Partenariat Hubert Curien") project funded over two years (extended with one more year) as well as financial support from the French Embassy in Malaysia, Université de Lorraine and Universiti Sains Malaysia.

# **CHAPTER 2**

# InGaN for Optoelectronics and Photovoltaics: Literature Review

This chapter comprehensively explores the fundamental properties inherent in the InGaN materials system, drawing upon an extensive range of literature reviews. Furthermore, the chapter delves into the advancements made in the application of InGaN material, specifically after the revision of InN bandgap in the early twenty-first century, which has demonstrated its remarkable capability to harness a broad spectrum of solar energy effectively. A specific focus is placed on the innovative utilization of InGaN in the field of photovoltaics, with an emphasis on its potential to achieve high efficiency. By examining these aspects and conducting a detailed analysis, the chapter aims to offer valuable insights into the properties and applications of InGaN, emphasizing its promising role in advancing photovoltaic technologies.

# 2.1 InGaN material systems for solar cells applications

III-nitride semiconductors, such as InGaN, hold a prominent status as the second most crucial group of semiconductors following Si [31]. This remarkable class of materials finds extensive utility in a diverse range of applications, including but not limited to LEDs, LDs, radio frequency (RF) communication, power amplifier, photovoltaic, and various other indispensable modern-day technologies. These materials have captivated researchers and innovators due to their distinct advantages over traditional Si or II-VI semiconductors [32]. The tuneable wide direct bandgap,

particularly in the case of InGaN, makes them exceptionally well-suited for optoelectronic and photovoltaic applications.

Additionally, their robust bonding enables them to operate reliably under high temperatures (> 400 °C [18], [19]), while their impressive breakdown voltages (> 35 V [33]–[35]) render them invaluable for high-power devices. Nevertheless, it is essential to note that the progress in material growth and device technology faces several challenges such as phase separation and composition inhomogeneities. In the following subsections, a comprehensive examination of all these aspects and their profound impacts on the field will be presented, offering in-depth understanding and analysis.

#### 2.1.1 Crystal structure

III-nitride semiconductors, such as GaN, InN and AlN, can crystallize in three primary polytypes: cubic zinc-blende, cubic rock-salt, and hexagonal wurtzite [36]. Among these, the wurtzite structure is the thermodynamically stable polymorph, while the zinc-blende and rock-salt structures are metastable under ambient conditions. The epitaxial growth of GaN and InN on cubic substrates such as Si [37]–[39], SiC [40], [41], and GaAs [42], [43] has successfully stabilized the zinc-blende crystal structure. This is achieved by leveraging the topological compatibility between the substrate and the material, overcoming the intrinsic tendency to form the wurtzite structure. On the other hand, the rock salt crystal structure in InN and GaN can only be induced under very high pressure and cannot be achieved through epitaxial growth process.

The reduction in lattice dimensions at high pressures promotes a more vital interionic Coulomb interaction, favouring the ionicity bonds over their covalent nature. Experimental observations have indicated that the structural phase transition to

the rock-salt structure occurs at estimated pressure values of approximately 12 GPa for InN [44] and 47 GPa for GaN [45]. Due to its distinctive crystal structure, rock-salt demonstrates an indirect bandgap and possesses a distinct phonon spectrum in contrast to zinc-blende and wurtzite structures. Both the wurtzite and zinc-blende lattice configurations exhibit a tetrahedral chemical bonds arrangement. However, their distinguishing characteristic lies in the stacking sequence of metal (group III) and nitrogen atoms within the close-packed diatomic planes.

As depicted in **Figure 2.1**, the wurtzite structure follows a hexagonal-closed packed (hcp) lattice with an alternating stacking sequence of AaBbAaBbAa..., while the zinc-blende structure adopts a face-centred cubic (fcc) lattice with a stacking sequence of AaBbCcAaBbCcAa... along the c-axis direction, respectively. The majority of III-nitride applications, including those discussed in this thesis, are based on the wurtzite structure. Therefore, the subsequent discussion will primarily focus on the properties and characteristics associated with the wurtzite structure.

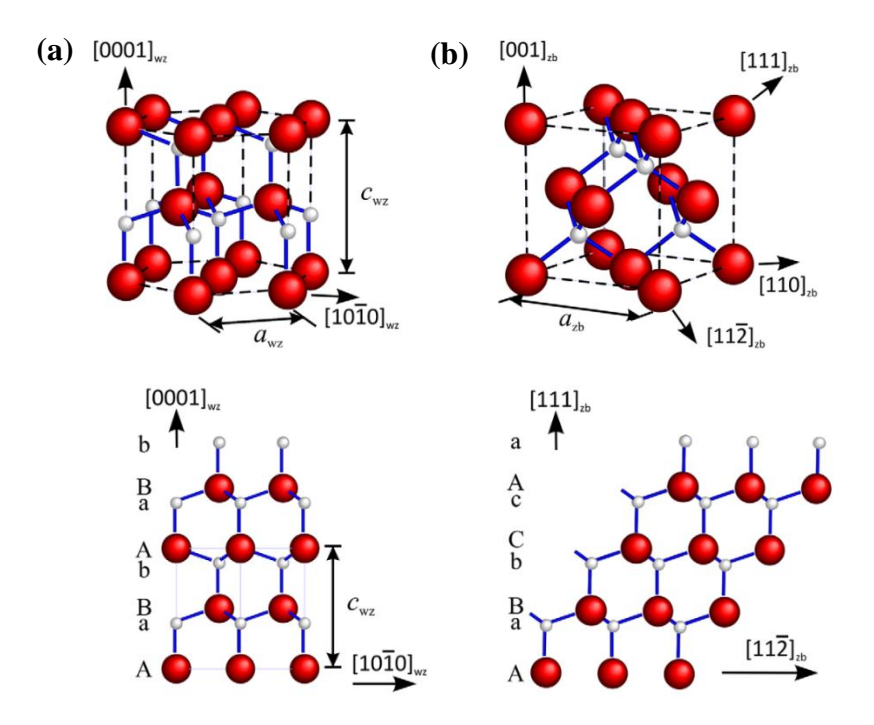


**Figure 2.1** Crystal structure of GaN polytypes with its different stacking sequence: (a) wurtzite  $(P6_3mc \text{ space group with } C_{6v}^4 \text{ symmetry})$  and (b) zinc-blende  $(F\overline{4}3m \text{ space group with } T_d^2 \text{ symmetry})$  [46].

In the context of hexagonal symmetry, the representation of crystal planes in III-nitride materials often employs the 4-axis Miller indices notation, which accounts for the sixfold symmetry exhibited by the wurtzite structure. This notation differs from the 3-index notation [hkl] typically used in the cubic system. In this notation, an additional index i is introduced, where the condition h + k = -i is applied, resulting in the notation [hkil]. In the wurtzite system, the hexagonal-compact lattice (hcp) is described by three parameters: the lattice constants a and b, and the internal parameter b, with its value summarized in **Table 2.1**. The lattice constant b corresponds to the distance between the hexagonal planes, while the lattice constant b represents the height of the unit cell along the b-axis.

**Table 2.1** III-nitride lattice parameter [47].

	AlN	GaN	InN	Unit
Lattice constant (a)	3.11	3.189	3.54	10 <sup>-8</sup> cm
Lattice constant (c)	4.98	5.185	5.70	10 <sup>-8</sup> cm
c/a ratio (ideal = 1.633)	1.601	1.626	1.616	-
u  (ideal = 0.375)	0.387	0.379	0.377	-
Spontaneous polarization	-0.81	-0.029	-0.032	C/m <sup>2</sup>

The internal parameter u determines the atomic displacement within the unit cell, specifically the bond length between the group-III cation and nitrogen anion along the c-axis direction and the degree of distortion within the unit cell. The quality or perfection of the wurtzite structure can be assessed by examining the value of the c/a ratio and u. In an ideal wurtzite structure, the c/a ratio and u are expected to have a value of 1.633 and 0.375, respectively. In the epitaxial growth of III-nitride materials however, it is commonly observed that the c/a ratio and u tend to deviate from its ideal

value. From a crystallographic perspective, this deviation from the ideal wurtzite structure is primarily influenced by the difference in electronegativity between the group III metal cation (Al, Ga, In) and the nitrogen anion.

The strong ionic bond between them causes the electron to displace from their equilibrium positions. This results in the development of an electron dipole moment along the c-axis orientation, contributing to the phenomenon known as spontaneous polarization. This characteristic has been widely utilized, such as in high-electron-mobility transistors (HEMTs) devices, where the electron can be confined within the two-dimensional electron gas (2DEG) at the AlGaN/GaN interface [48], [49]. Additionally, as a result of the non-centrosymmetric characteristics of the wurtzite structure, III-nitrides display two distinct polarities based on the alignment of the group III metal cation and nitrogen anion along the c-axis [0001] direction [50]. III-polar (III-faced) refers to the orientation where the III-N bond faces the +c [0001] direction, while N-polar (N-faced) indicates the arrangement where the III-N bond aligns with the -c [0001] direction.

The structure of InGaN polarities is shown in **Figure 2.2**. The polarity of the grown III-nitride structure can be controlled by manipulating the growth condition. However, it is important to note that when using techniques such as MOCVD and MBE, the majority of III-nitride growth tends to thermodynamically favor in III-polar due to lower absolute surface free energy compared to N-polar [51]. Typically, the epitaxial growth of N-polar structures is often accompanied by hillock morphology due to slower growth kinetics (large surface energy), which poses challenges in achieving an abrupt interface, especially in thickness-sensitive structures, such as MQWs and SLs [52].

Moreover, the III-nitride compound exhibit a continuous alloy system with a tuneable wide direct bandgap, which can be engineered within a range of 0.67 eV (InN) to 3.4 eV (GaN) and all the way up to 6.1 eV (AlN). Hence, this class of materials offers exceptional versatility in accommodating a wide range of spectral wavelengths, effectively covering from the infrared region (~1770 nm) into the far ultraviolet region (~200 nm). One prominent example is the In<sub>x</sub>Ga<sub>1-x</sub>N ternary alloy system, which demonstrate a wide range of tuneable direct bandgaps that encompass a significant portion of the solar spectrum, including the entirety of the visible range, simply by manipulating the indium composition, as depicted in **Figure 2.3**.

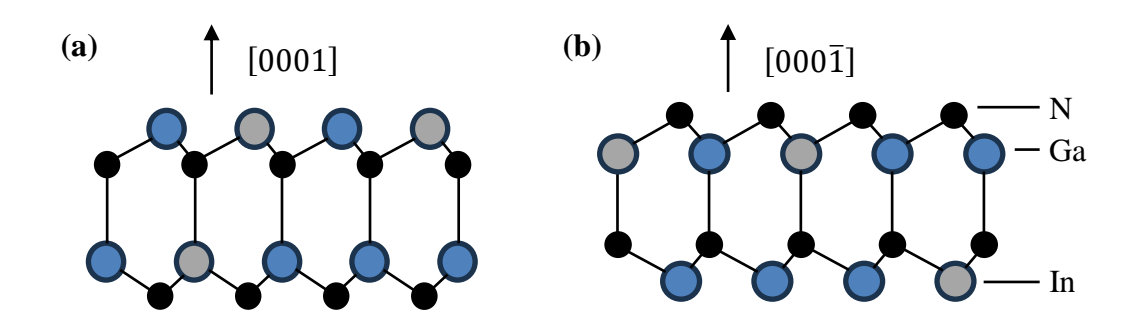


**Figure 2.2** Crystal structure of InGaN polarity [53]: (a) III-polar and (b) N-polar.

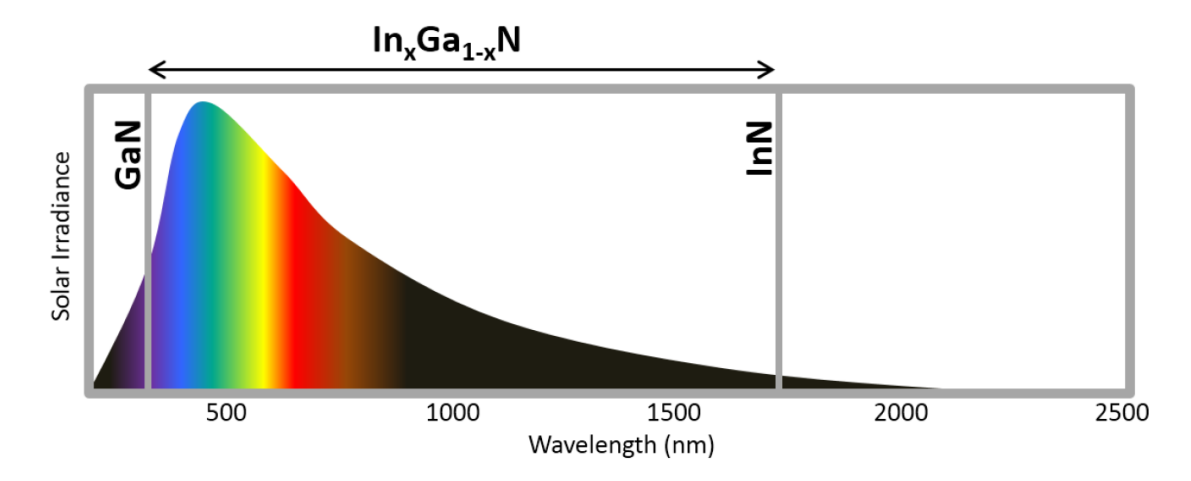


**Figure 2.3** AM0 solar spectrum as a function of spectral wavelength and its correlation with InGaN bandgap (from 0.7 eV (1770 nm) to 3.4 eV (360 nm)), showing that this ternary is almost perfectly matched with the solar spectrum simply by manipulating indium composition.

This characteristic renders  $In_xGa_{1-x}N$  alloys well-suited for various applications particularly in optoelectronic devices such as LEDs, LDs and photovoltaics. The renounce interest in  $In_xGa_{1-x}N$  alloys system came after the revision of the InN fundamental bandgap from 1.9 eV to 0.67 eV in the early  $21^{st}$  century. The variation in the bandgap value can be attributed to the Burstein-Moss effect, as described by Wu et al. [54]. This effect causes the absorption edge to shift to higher energies (shorter wavelengths) as the doping concentration increases. Early studies on InN often utilized sputtering as the growth technique, which could unintentionally introduce high concentrations of oxygen into the material. Oxygen acts as a donor in InN, leading to a high electron concentration within the films, reaching levels up to  $10^{20}$  cm<sup>-3</sup>.

The presence of a large number of free electrons causes the Fermi level to shift deep into the conduction band, following non-parabolic trajectory as shown in **Figure 2.4.** This resulted in a higher observable optical bandgap as reported in early studies. In the case of III-nitride ternary alloys  $(A_xB_{1-x}N)$ , the bandgap does not change linearly with the alloy composition, x. Instead, it follows a non-linear relationship. One common expression used to describe the variation of the bandgap with composition is the modified Vegard's relation, which is given by:

$$E_g^{A_x B_{1-x} N}(x) = x E_g^{AN} + (1-x) E_g^{BN} - bx(1-x)$$
 Eq. 2.1

where b is the bowing parameter. The bowing parameter is used to quantify the deviation from the Vegard's relation, which is the linear interpolation between the bandgaps of the binary components in an alloy. It indicates the degree of non-linearity and can be either positive (downward bowing) or negative (upward bowing), depending on the specific alloy system.

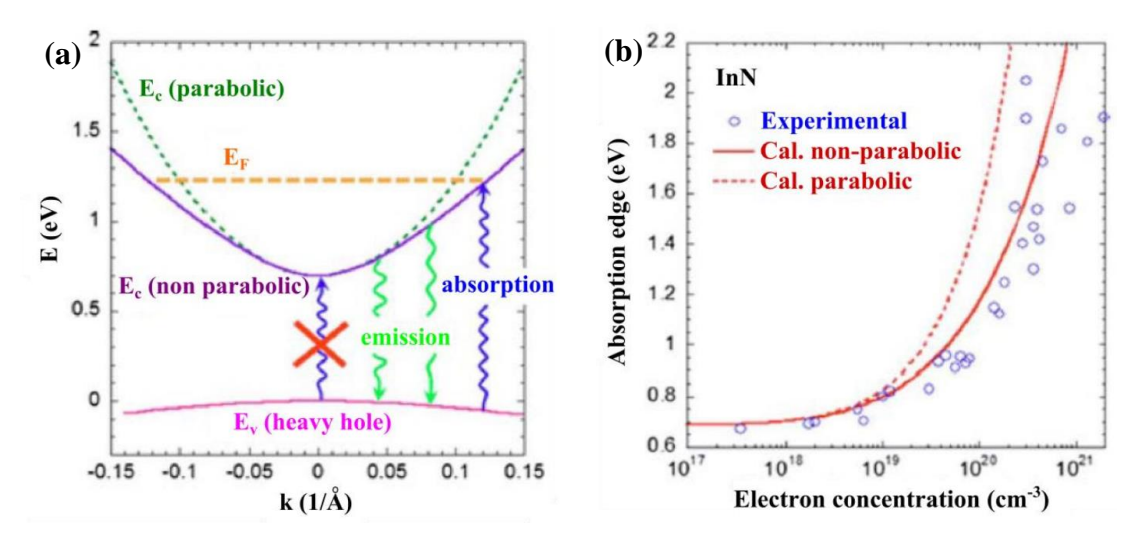


**Figure 2.4** (a) Calculated valence and conduction band curve of InN based on theoretical k.p model and (b) experimental and absorption edge of InN following the experimental and theoretical value according to parabolic and non-parabolic conduction band [55].

In the case of the InGaN alloy, accurately determining the bowing parameter value across the entire composition range remains an active area of research and is subject to ongoing debate. Experimental investigations and theoretical studies have reported a range of values for b, typically varying from 1.2 to 4 eV [56]–[61]. This variation can be influenced by factors, such as measurement techniques and the quality of the grown material (growth method and defect density). Notably, Moses et al. proposed that the specific value of the bowing parameter in InGaN strongly depends on the indium composition within the alloy [62]. An increase in the indium composition can induce hole localization due to alloy disordering, leading to a significant Stokes shift occurs within the epitaxial layer [63], [64].

Consequently, the bandgap for a given indium composition may be underestimated, especially when measured using photoluminescence (PL) techniques. Moreover, Vegard's law can be implemented in high-resolution X-ray diffraction (HR-XRD) analysis in determining the indium composition within the InGaN epitaxial layer. However, the validity of Vegard's law is limited to relaxed lattice parameters

where there is no strain present. In HR-XRD, the lattice constant along the c-axis is typically measured, and the indium composition in the InGaN layer can be determined by applying Vegard's law, which involves linear interpolation between the lattice constants of binary InN and GaN. However, when InGaN layers experience biaxial compression, the unit cell becomes distorted, resulting in an elongation of the lattice constant along the c-axis. This leads to a systematic overestimation of the indium composition.

Therefore, it is crucial to assess the composition of InGaN alloys not only through XRD but also through other means of analysis as an independent reference, such as Rutherford backscattering spectroscopy (RBS), secondary ion mass spectroscopy (SIMS), transmittance and photocurrent measurement.

#### 2.1.2 Physical properties

In addition to its tunable bandgap, InGaN also exhibits exceptional radiation tolerance, exhibiting irradiation-induced degradation in PL intensity at levels below 0.1 decade/10<sup>12</sup> [20] with a predicted lifespan of over 30 years under solar storm proton irradiation [18]. The robustness of InGaN against radiation-induced damage can be understood by examining the energy placement of Fermi stabilization levels (E<sub>FS</sub>) within the charge transition state of the binary compounds GaN and InN, as proposed by Walukiewicz et al. [65] and Li et al. [66]. This relationship is illustrated in **Figure 2.5**. The E<sub>FS</sub> is associated with native defect exhibits within the grown structure, including broken bond or vacancies defects, generated by high-energy proton irradiation.

When the  $E_{FS}$  is positioned near the mid-gap position, the generated defects tend to function effectively as non-radiative recombination centres. This phenomenon

accounts for the sensitivity of materials like GaAs and GaInP to native defects, leading to performance degradation in applications such as LEDs and photovoltaics. In contrast, in the case of InN, the E<sub>FS</sub> is situated deep within the conduction band. The presence of high energy barriers inhibits carrier recombination through radiation-induced defect states. Consequently, these defects are less efficient as centres for recombination in charge transition states. Thus, by increasing the indium composition within InGaN epilayer, the overall structure is anticipated to become more resilient to radiation-induced damage.

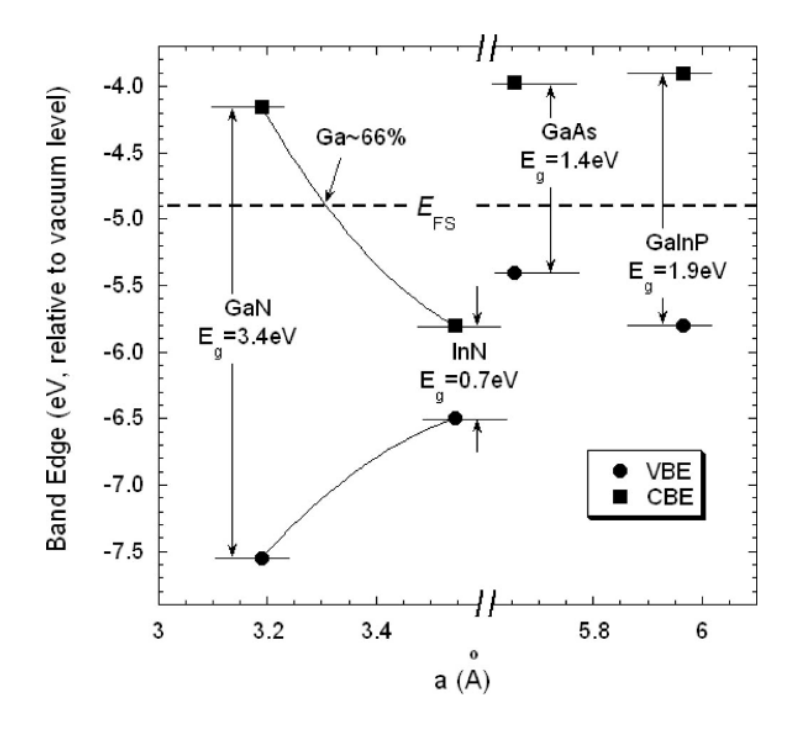


**Figure 2.5** The E<sub>FS</sub> position in relation to conduction band maxima and valence band minima of GaN, InN, GaAs and Ga<sub>0.5</sub>In<sub>0.5</sub>P [66].

Furthermore InGaN is also recognized for its remarkable temperature tolerance, boasting an exceptional operational range of up to 400 °C [18], [19]. In a study conducted by Huang et al., the influence of temperature (ranging from room temperature to 450 °C) on nonpolar InGaN-based solar cells was investigated. The findings indicated that the cell displayed a substantial positive temperature coefficient from room temperature up to 350 °C [67].

InGaN is also characterized by its high absorption coefficient, reaching magnitudes of up to 10<sup>5</sup> cm<sup>-1</sup> at the band edge, across all composition range (from 365 nm to 1850 nm) [16]. This distinctive property allow that nearly 90% of incident photons are absorbed within the initial 120 nm of an InGaN film [68]. The high absorption coefficient enables the development of InGaN-based solar cells to be carried out on relatively thin structure, thereby reducing the associated material costs. Moreover, InGaN also possess high carrier mobility with the experimental value exceeding 300 cm<sup>2</sup>/Vs [17]. The high carrier mobility facilitates the efficient transport of the photo-generated carriers across the junction and minimizing losses due to recombination.

It worth to note that, the relatively low toxicity of InGaN compared to other semiconductors (with e.g., arsenic, cadmium, or phosphorous) makes its processing and disposal environmentally favourable. This distinctive attribute highlights the potential utility of InGaN-based solar cells in the area of high-efficiency photovoltaic devices. These applications encompass concentrator photovoltaics, photovoltaic-thermal systems, or space application where the ability to operate in harsh environment (elevated temperature and radiation exposure) is important. In such scenarios, InGaN-based solar cells could offer advantages over conventional Si or III-V photovoltaic devices. The physical properties of binary III-nitride are summarized in **Table 2.2**.

**Table 2.2** Physical properties related to the binary of III-nitride [69]–[71].

Hexagonal (wurtzite)	AlN	GaN	InN	Unit
Density	3.23	6.15	6.81	g cm <sup>-3</sup>
Bandgap ( $E_g$ ) at 300 K	6.2	3.39	0.64	eV

Temperature	-	-6	-1.8	10 <sup>-4</sup> eV K <sup>-1</sup>
dependence				
Pressure dependence	-	4.2	-	10 <sup>-3</sup> eV
				kbar <sup>-1</sup>
Thermal expansion	$\Delta a/a = 4.2$	$\Delta a/a = 5.59$	$\Delta a/a \sim 4$	10 <sup>-6</sup> K <sup>-1</sup>
coefficient				
	$\Delta c/c = 5.3$	$\Delta c/c = 3.17$	$\Delta c/c \sim 3$	10 <sup>-6</sup> K <sup>-1</sup>
Deformation potential	9.5	8.3	7.1	eV
Thermal conductivity	2	1.3	0.8	W cm <sup>-1</sup> K <sup>-1</sup>
Refractive index	2.15 (3 eV)	2.33 (1 eV)	2.9 - 3.05	-
	-	2.67 (3.38 eV)	-	-
Dielectric constant	$\varepsilon_{\infty} = 4.77$	$\varepsilon_{\infty} = 5.35$	$\varepsilon_{\infty} = 8.4$	-
	$\varepsilon_0 = 8.5$	$\varepsilon_0 = 8.9 - 9.5$	$\varepsilon_0 = 15.3$	-
Electron effective mass	0.48	0.2	0.11	$m_O$
Electron saturation	1.4	2.5	2.5	$10^7  \text{cm s}^{-1}$
velocity				
Breakdown field	-	>5	-	10 <sup>6</sup> V s <sup>-1</sup>

# 2.1.3 Limitations and challenges

### 2.1.3(a) Growth process

While high indium composition in InGaN alloys allows for a broader bandgap tunability and extends the range of absorption wavelengths, it also introduces several difficulties in material growth and device fabrication. When it comes to the epitaxial

growth of InGaN-based structure, two primary techniques are commonly employed, which are metalorganic chemical vapor deposition (MOCVD) and molecular beam epitaxy (MBE). These techniques allow precise control over the growth of InGaN materials with desired composition and crystal quality. MOCVD involves the epitaxial growth of thin films by introducing metalorganic precursors and carrier gas into a heated reactor chamber. Under controlled conditions, the precursors decompose and react to form the desired InGaN layers on a substrate. MOCVD offers high growth rates, excellent uniformity, scalability, and multi-wafer growth.

The development of InGaN using the MOCVD technique has undergone significant development, particularly in LED devices in the ultraviolet to the green spectral range [72]–[74]. MBE, on the other hand, relies on the precise deposition of individual atoms or molecules onto a substrate in ultra-high vacuum conditions. By carefully controlling the flux of the constituent elements, epitaxial growth of InGaN layers can be achieved with atomic precision. MBE is known for its superior control over layer thickness, composition, and interface quality but with a drawback such as low growth rate and low output. Even though MOCVD and MBE are the dominant growth techniques for InGaN-based solar cells, there are also limited reports of using a sputtering method for the fabrication of InGaN materials for photovoltaic applications [75].

The main objective in developing any composite materials, including InGaN, is to achieve a homogeneous distribution of elements throughout the grown structure. Studies have reported the successful growth of high-quality monocrystalline InGaN epitaxial layers with indium compositions up to 15% using MOCVD technique [76], [77]. However, achieving higher indium compositions in InGaN remains challenging due to a large lattice mismatch between InN and GaN (10.7% and 15.0% for a and c

lattice constant along the c-axis direction, respectively). The lattice mismatch results in significant internal strain within the structure, causing a distortion within the crystalline lattice. Consequently, a miscibility gap will occur within a specific range of the alloy mixture.

Within this gap, the thermodynamically unstable InGaN alloy undergoes spontaneous spinodal decomposition, wherein distinct thermodynamically stable phases form without the need for nucleation or overcoming interfacial energy barriers, allowing the distribution of the In-rich phase at the In-deficit region in a spatially random manner. According to the thermodynamic analysis conducted by Figge et al. [78] in accordance with the calculation from Stringfellow [79] and Karpov [80] using valence-force-field (VFF) model, the behaviour of the spinodal and binodal lines in InGaN differs between relaxed and pseudo-morphically strained structure. The binodal line represents the boundary that distinguishes conditions where a single-phase system is thermodynamically favourable from conditions where phase separation into distinct phases becomes favourable.

Below the binodal line lies the spinodal region, where the alloy can undergo barrierless phase separation into distinct phases with different properties due to thermodynamic instabilities. Based on the theoretical pseudo-binary GaN-InN phase diagram suggested by Figge et al. as shown in **Figure 2.6**, it is found that for relaxed structures, in order to achieve a stable InGaN alloy at a typical growth temperature of 800 °C, the maximum indium composition should be limited to 10% or lower. Beyond this composition, the InGaN system becomes increasingly unstable, and phase separation through spinodal decomposition is likely to occur. On the other hand, for fully strained structures with respect to the GaN template, the phase diagram suggests that a thermodynamically stable InGaN with an indium composition of up to 50%